Journal of Ceramic Processing Research. Vol. 12, No. 2, pp. 160~164 (2011)

J O U R N A L O F
Ceramic Processing Research

Synthesis by a PECVD technique and mechanical properties of nc-Ti(B,N)/a-BN coatings

Kwang Soo Choi[a], Young Su Hong[a], Se Hun Kwon[b], Jihwan Choi[b], Qi Min Wang[b] and Kwang Ho Kim[a,b,*]

[a]*School of Materials Science and Engineering, Pusan National University, Busan 609-735, South Korea*

[b]*National Core Research Center for Hybrid Materials Solution, Pusan National University, Busan 609-735, South Korea*

Ternary Ti-B-N coatings with different B contents were deposited on AISI 304 stainless steel substrates and Si wafers using a plasma enhanced chemical vapor deposition (PECVD) technique in a gaseous mixture of $TiCl_4$, BCl_3, H_2, N_2 and Ar. The chemical composition, microstructure and mechanical properties of the Ti-B-N coatings were systematically investigated. The results indicated that the B contents significantly affected the microstructure and mechanical properties of Ti-B-N coatings. An increase of the B content in the coatings resulted in a decreased grain size and a finer microstructure. At a B content of 11.41 at.%, the coating exhibited a nanocomposite microstructure consisting of Ti(B,N) nanocrystals and a surrounding amorphous BN tissue phase. At this B content, the highest microhardness of ~38 GPa was reached. With a further increase in the B content, the microhardness of the coatings decreased. Lower friction-coefficients were also observed due to B additions in the coatings.

Key words: Ti-B-N, nano-composite, PECVD, Boron content, Microhardness, friction coefficient.

Introduction

Titanium nitride (TiN) coatings have been widely applied on cutting tools, forming dies, bearings, etc [1-3]. In order to meet the increasing need for superior mechanical properties and high temperature stability, the addition of a third element has been widely investigated, such as Ti-Al-N, Ti-Si-N, Ti-C-N, and Ti-B-N coatings. These ternary coatings exhibited higher hardness, a lower friction coefficient, or improved oxidation resistance [4-7].

By adding B into TiN, two- or three-phase coatings containing the nanocrystalline (nc-) Ti(B, N) and amorphous (a-) tissue phases of a-TiB_2, or a-TiB + a-BN, or a-TiB_2 + a-BN were formed [8-11]. These Ti-B-N nanocomposite coatings have attracted great attention in recent years because of their excellent properties, such as super hardness, high toughness, chemical inertness and good thermodynamic stability at high temperature [8-13].

Ti-B-N coatings have been synthesized using magnetron sputtering [8, 11, 12], cathodic arc evaporation (CAE) [7, 10, 11, 13], and plasma enhanced CVD (PECVD) techniques [8, 9]. The coatings were mainly of nc-TiN/a-TiB_2, nc-TiN/(a-TiB_2, BN) or nc-TiN/(a-TiB, BN) nanocomposites [8-13]. Systematic investigations on nanocomposite coatings containing only nc-TiN and a-BN phases were rarely reported. In this study, we synthesized the Ti-B-N coatings in the compositions of the TiN-BN phases. The influence of B additions on the coating microstructure and a nc-TiN/a-BN nanocomposite coating with much improved mechanical properties is reported.

*Corresponding author:
Tel : +82-51-510-2391
Fax: +82-51-510-3660
E-mail: kwhokim@pusan.ac.kr

Experimental Details

Ternary Ti-B-N coatings were deposited on AISI 304 stainless steel substrates and Si wafers by a PECVD technique using a gaseous mixture of $TiCl_4$, BCl_3, H_2, N_2 and Ar. A schematic diagram of our PECVD apparatus is depicted in Fig. 1. The deposition chamber consisted of a vertical quartz tube with a diameter of 55 mm and length of 500 mm. A coil for the inductively coupled plasma (ICP) surrounded the outer wall of the quartz tube and was connected to an RF source of 13.56 MHz. A graphite susceptor was located inside the chamber and was heated

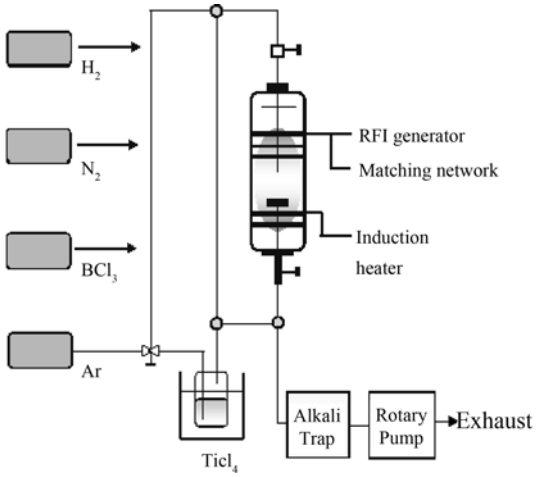

Fig. 1. Schematic diagram of the RF-PECVD experimental apparatus.

by an induction coil using a high-frequency source of 115 kHz. The gaseous mixture of $TiCl_4$, BCl_3, H_2, N_2 and Ar was passed downstream through a nozzle made of stainless steel. The inlet amount of $TiCl_4$ vapor was controlled by varying both the evaporating pressure of $TiCl_4$ and the amount of carrier Ar gas passing an evaporator. The evaporator for $TiCl_4$ was maintained at 0 °C to obtain a suitable vapor pressure. The flow rates of all the gases were individually controlled with mass flow controllers. Ti-B-N coatings with different B contents were deposited by varying the input gas ratio (R_x), $R_x = [BCl_3/(BCl_3 + TiCl_4)] \times 100$ [14]. The typical deposition conditions for Ti-B-N coatings were listed in Table 1.

The chemical compositions and bonding status of the Ti-B-N coatings were analyzed using an electron probe microanalyzer (EPMA 1600, Shimadzu) and X-ray photoelectron spectroscopy (XPS, VG Scientifics, ESCALAB 250), respectively. An X-ray diffractometer (XRD, D8, Bruker) were utilized to investigate the phase structure of the Ti-B-N coatings using the standard Bragg-Brentano geometry with Cu-$K\alpha$ radiation. The surface and cross-sectional morphologies of the coatings were observed using a field emission scanning electron microscope (S 4800, Hitachi). The film thicknesses were determined from fractured cross-sectional SEM images. Cross-sectional transmission electron microscopy (TEM) images were obtained from a selected sample. A field emission transmission electron microscope (FE-TEM, JEOL, JEM-400FX) operated at an acceleration voltage of 400 KV was used. The sample was prepared by milling in a focused-ion-beam system.

The hardness was evaluation using a microhardness tester with a Knoop indenter (Matsuzawa, MMT-7) under a load of 25 gf. The friction coefficient was evaluated through sliding ware tests using a conventional ball-on-disk wear apparatus. A steel ball (diameter 6.34 mm, 700 $Hv_{0.2}$) was used as a counterpart material. The sliding tests were conducted with a sliding speed of 0.157 m/s under a load of 5 N at ambient temperature (around 24 °C) and a relative humidity of 25-30%.

Results and Discussion

Microstructure of Ti-B-N coatings

By varying the input gas ratio (R_x) from 0% to 88%, $R_x = [BCl_3/(BCl_3 + TiCl_4)] \times 100$, Ti-B-N coatings with different B contents were deposited. Similar results have been reported in PECVD Ti-B-C-N coatings [14]. Fig. 2 gives the chemical compositions of the Ti-B-N coatings determined by EPMA in the Ti-B-N phase diagram [13]. The data points are almost on the TiN-BN tie line, with B contents ranging from 0 to 19.21 at.%. The Ti+B and N contents remained almost unchanged. The residual Cl content in the coatings was maintained at ~1 at.%.

Fig. 3(a) shows XRD patterns of the Ti-B-N coatings.

Table 1. Typical deposition parameters for the Ti-B-N coatings

Total flow rate	70 sccm
Working gas ratio[N_2/H_2/Ar]	6/34/30 sccm
Deposition pressure	133.3 Pa
Deposition time	1 h
R.F. power	180 W
Deposition temperature	600 °C
Input gas ratio, Rx = $[BCl_3/(BCl_3 + TiCl_4)] \times 100$	0~100%

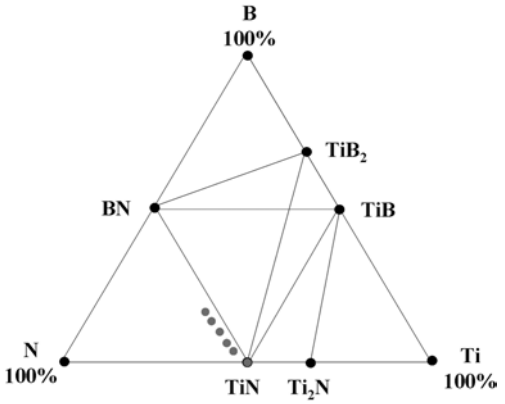

Fig. 2. Simplified phase diagram of the Ti-B-N system. Circles indicate the chemical compositions of the Ti-B-N coatings deposited with varying gas ratios.

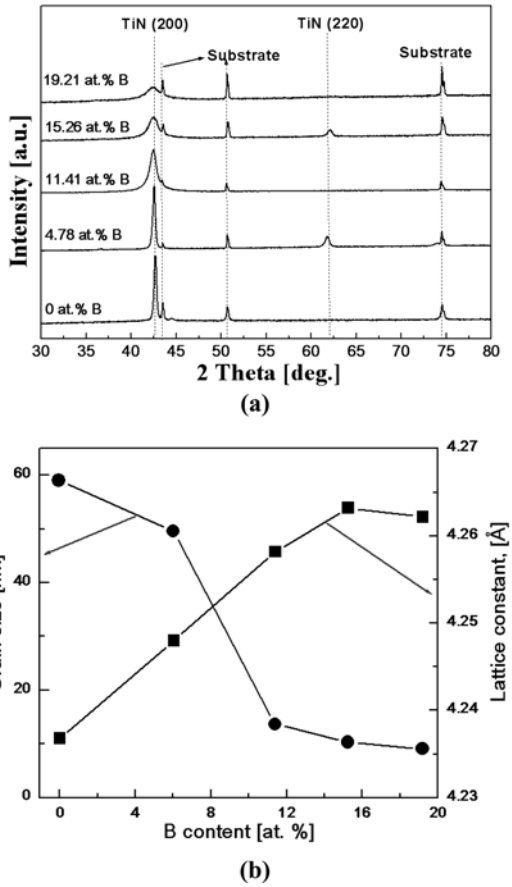

Fig. 3. (a) XRD patterns of TiB_xN (x = 0, 4.78 at.%, 11.41 at.%, 15.26 at.%, and 19.21 at.%) coatings and (b) grain sizes and lattice constants of TiN phase in the Ti-B-N coatings as a function of the B content calculated using FWHM and position of the TiN (200) peaks.

All the diffractions peaks of the coatings were from the FCC-TiN phase, with (200) preferred orientations being observed. No phase related to B was identified. Increasing the B content in the Ti-B-N coatings resulted in apparent broadening and shift of the TiN (200) peak. Fig. 3(b) summarizes the grain sizes and lattice constants calculated from full width of the peak at half maximum intensity (FWHM) and position of TiN (200) diffraction peaks using Bragg's formula and the Scherrer equation, respectively [15, 16]. The lattice constant values increased gradually with increasing B content in the Ti-B-N coatings and reached a saturated value when the B content was larger than 15.26 at.%. As compared to the standard value (4.241 Å, JCPDS 38-1420), the lattice constants of the TiN phase in the B-containing coatings were larger. The variation of the lattice constants can be attributed to a solid solution of B in the TiN phase. The atomic radius of the B atom is larger than that of N atom. Therefore, the substitution of N atoms by B atoms in the TiN phases resulted in an expansion of the crystalline lattices. Similar phenomena have been reported in other investigations [17, 18]. The saturation of lattice constant values at a B content above 15.26 at.% indicated a limited solid solubility of the B element in the FCC-Ti(B, N) phase. From Fig. 3(b), it was also revealed that the grain size of the FCC-Ti(B, N) phase decreased gradually from approximately 59 nm to 9 nm with an increase in the B content from 0 to 19.2 at.%.

Fig. 4 and Fig. 5 show surface and cross-sectional FE-SEM images of the Ti-B-N coatings with various B contents, respectively. Consistent with the results of grain size calculations in Fig. 3(b), decreases in the grain size were observed with an increase in the B content. In the B-free TiN coatings, apparent columnar grains with faceted tops were observed (Fig. 4(a) and Fig. 5(a)). The B containing Ti-B-N coatings exhibited much finer microcolumnar microstructures with an increase in the B content (Figs. 4(b)-(d) and Figs. 5(a)-(d)).

To investigate the chemical bonding status in the Ti-B-N coatings, The Ti-B(11.41 at.%)-N coating was examined

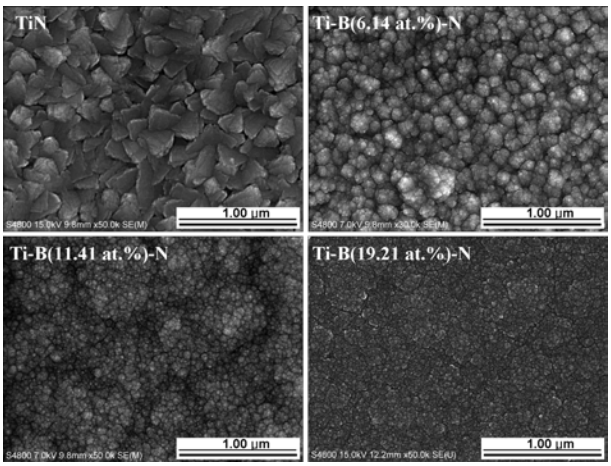

Fig. 4. Surface FE-SEM images of Ti-B-N coatings with various B contents. (a) TiN, (b) Ti-B(6.14 at.%)-N, (c) Ti-B(11.41 at.%)-N, and (d) Ti-B(19.21 at.%)-N.

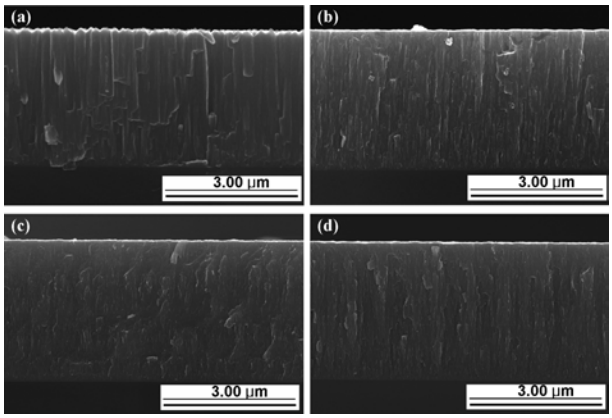

Fig. 5. Cross-sectional FE-SEM images of (a) TiN, (b) Ti-B(6.14 at.%)-N, (c) Ti-B(11.41 at.%)-N, and (d) Ti-B(19.21 at.%)-N coatings.

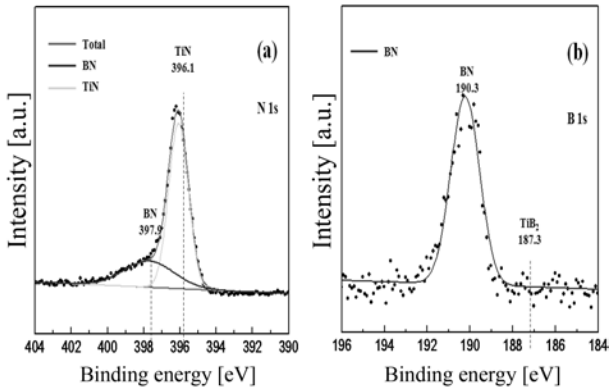

Fig. 6. XPS spectra near the binding energy of (a) N1s and (b) B1s for a Ti-B(11.41 at.%)-N coating.

by X-ray photoelectron spectroscopy (XPS). The binding energies were calibrated with the C 1s peak at 284.5 eV as a reference. Fig. 6 shows the Ti-B(11.41 at.%)-N XPS spectra near the binding energies of (a) N 1 s and (b) B 1 s. In the case of N1s (Fig. 6(a)), the TiN and BN phase peaks corresponding to 396.1 eV and 397.9 eV were observed respectively [19]. As shown in Fig. 6(b), only one peak corresponding to 190.3 eV was also observed, which is in good agreement with that of the BN phase [19]. No peak corresponding to TiB_2 (187.3 eV) was detected. The XRD and XPS results in Fig. 3 and Fig. 6 indicated that the B element in the Ti-B(11.41 at.%)-N coating existed in both a crystalline Ti(B,N) solid-solution and an amorphous BN phase.

Fig. 7 shows a cross-sectional dark-field TEM image, a selected area diffraction pattern (SADP) and a high-resolution (HR-) TEM images of the Ti-B(11.41 at.%)-N coating. As shown in Fig. 7(a), the nano-sized Ti(B,N) crystals were distributed uniformly in the matrix. The SADP image in the inset in Fig. 7(a) indicates the unclear diffraction rings corresponding to very fine nanocrystals. Crystal orientations (111) and (220) of the Ti(B, N) also existed, which were not observed in the XRD results (Fig. 3(a)). The HR-TEM image in Fig. 7(b) shows clearly the nano-

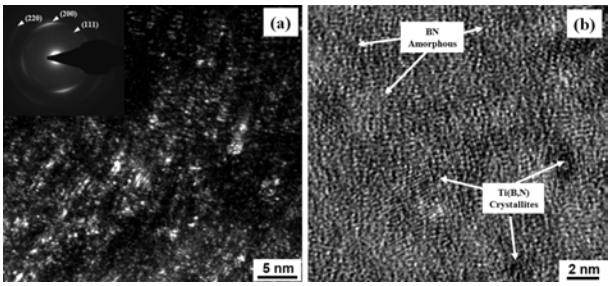

Fig. 7. (a) DF-TEM image (with SADP in inset) and (b) HR-TEM image of Ti-B(11.41 at.%)-N coating.

compostie microstructure containing lattice fringes of the nanocrystals and the amorphous matrix phase. By combining the XRD results (Fig. 3) and XPS results (Fig. 6), it can be concluded that the nanocrystals are the Ti(B, N) phase while the amorphous matrix is a-BN.

Based on the results from XRD, XPS, SEM, and TEM results, it is clear that the B additions to the TiN coatings resulted in crystallite size refinement. At a B content of 11.41 at.%, the coating exhibited a nano-composite structure consisting of Ti(B, N) nanocrystals surrounded by an amorphous BN tissue phase. The formation of the nano-composite in the Ti-B-N coatings was related to the spinodal phase segregation due to immiscibility between TiN and BN phases [20].

Mechanical properties of Ti-B-N coatings

Fig. 8 shows the microhardness of the Ti-B-N coatings as a function of the B content. As B was added in the TiN coating, higher microhardness values were found. In this study, the highest value of microhardness was 38 GPa at a B content of 11.41 at.%. This result can be explained by the grain boundary hardening created by a strong cohesive energy of interphase boundaries between nanosized Ti(B,N) crystals and the amorphous BN phase, which restrains grain boundary sliding [21], and by a Hall-Petch relation derived from crystal size refinement [22]. On the other hand, the microhardness rebounded when the B content was increased above 11.41 at.%. The value decreased to ~23.4 GPa at a B content of 19.21 at.%, which is related to the increase of the relatively soft a-BN phase.

Fig. 9 shows the friction-coefficients of the Ti-B-N coatings evaluated by a ball-on-disk wear sliding tester. The average friction coefficient of the TiN coatings was ~0.52. As the B content increased to 11.4 at.% and 15.26 at.%, the average friction coefficients of the Ti-B-N coatings decreased to ~0.45 and ~0.41, respectively. In the Ti-B-N coatings, the amorphous BN took the role of a lubricant [23], which resulted in a decrease of the friction coefficient. Also BN might react with ambient H_2O to produce B_2O_3 through a tribo-chemical reaction, which can act as a self lubricant layer [24, 25].

Conclusions

Ternary Ti-B-N coatings with various B contents were deposited on AISI 304 stainless steel substrates and Si wafers by a PECVD technique using a gaseous mixture of $TiCl_4$, BCl_3, H_2, N_2 and Ar. The B content significantly affected the microstructure and mechanical properties of Ti-B-N coatings:

(1) The chemical compositions of the Ti-B-N coatings were close to the TiN-BN tie line in the Ti-B-N phase diagram. Only the FCC-TiN phase with a solid solution of B elements were identified in the XRD patterns. The B element existed in the solid solutions of Ti(B, N) or amorphous BN phases.

(2) An increase of the B content in the coatings resulted in a decreased grain size and finer microstructures. B-free TiN coatings were observed to have an apparent columnar grain with faceted tops (Fig. 4(a) and Fig. 5(a)). The B

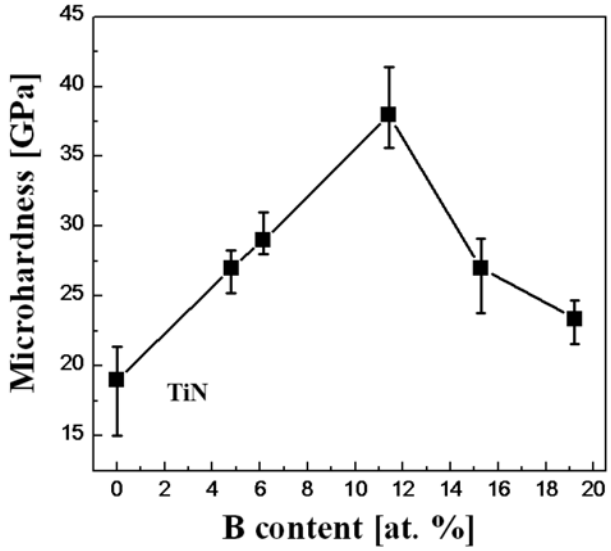

Fig. 8. Microhardness of Ti-B-N coatings as a function of the B content.

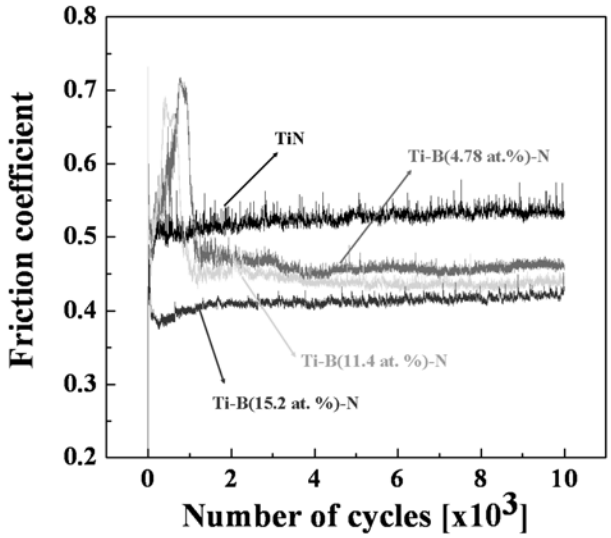

Fig. 9. Average friction coefficient of Ti-B-N coatings with various B contents.

containing Ti-B-N coatings exhibited much finer nano-columnar microstructures with an increase of the B content.

(3) At a B content of 11.41 at.%, the coating exhibited a nanocomposite microstructure consisting of Ti(B, N) nano-crystals with a surrounding amorphous BN tissue phase.

(4) An increase of the B content in the Ti-B-N coatings resulted in first an increase and then rebounding of the microhardness values. The peak microhardness was observed to be ~38 GPa at a B content of 11.41 at.%, corresponding to a nanocomposite microstructure in the coating. Lower friction-coefficients were also observed due to B additions in the coatings.

Acknowledgement

This research was supported by NCRC (National Core Research Center) program through the National Research Foundation of Korea funded by the Ministry of Education, Science and Technology (2010-0001-226).

References

1. A. Kawana, H. Ichimura, Y. Iwata and S. Ono, Surf. Coat. Technol. 86-87 (1996) 212-117.
2. M.R. Hilton, L.R. Narasimhan, S. Nakamura, M. Salmeron and G.A. Somorjai, Thin Solid Films 139[3] (1986) 247-260.
3. R. Makabe, S. Nakjima and O. Tabata, Thin Solid Films 137[1] (1986) 49-50.
4. C.W. Kim and K.H. Kim, Thin Solid Films 307 (1997) 113-119.
5. K.H. Kim, S. Choi and S. Yoon, Surf. Coat. Technol. 161[2-3] (2002) 243-248.
6. E.Y. Choi, C.S. Jang, M.C. Kang and K.H. Kim, Solid State Phenomena 118 (2006) 311-315.
7. Y. Tanno and A. Azushima, Surf. Coat. Technol. 203[23] (2009) 3631-3637.
8. P. Karvankova, M.G.J. Veprek-Heijman, O. Zindulka, A. Bergmaier and S. Veprek, Surf. Coat. Technol. 163-164 (2003) 149-156.
9. P. Karvankova, M.G.J. Veprek-Heijman, D. Azinovic and S. Veprek, Surf. Coat. Technol. 200[9] (2006) 2978-2989.
10. Y.H. Lu, Y.G. Shen and K.Y. Li, Appl. Surf. Sci. 253[3] (2006) 1631-1638.
11. Y.H. Lu, Y.G. Shen, J.P. Wang, Z.F. Zhou and K.Y. Li, Surf. Coat. Technol. 201[16-17] (2007) 7368-7374.
12. P.H. Mayrhofer and M. Stoiber, Surf. Coat. Technol. 201[13] (2007) 6148-6153.
13. J. Neidhardt, Z. Czigány , B. Sartory, R. Tessadri, M. O'Sullivan and C. Mitterer, Acta Mater. 54[16] (2006) 4193-4200.
14. K.H. Kim, J.T. Ok, S. Abraham, Y.-R. Cho, I.-R. Park and J.J. Moore, Surf. Coat. Technol. 201[7] (2006) 4185-4189
15. I.-W. Park, S.R. Choi, M.-H. Lee and K.H. Kim, J. Vac. Sci. Technol. A 21[4] (2003) 895-899.
16. A. Jung, H. Natter, R. Hempelmann and E. Lach, J. Mater. Sci. 44[11] (2009) 2725-2735.
17. C. Pfohl, A. Gebauer-Teichmann and K.-T. Rie, Surf. Coat. Technol. 112[1-3] (1999) 347-350.
18. C. Pfohl and K.-T. Rie, Surf. Coat. Technol. 116-119 (1999) 911-915.
19. J.F. Moulder, W.F. Stickle, P.E. Sobol and K.D. Bomben, in "Handbook of X-ray Phothoelectron Spectroscopy", (Physical Electronics Inc., 1995) p. 213.
20. R.F. Zhang, S.H. Sheng and S. Veprek, Acta Mater. 56[16] (2008) 4440-4449.
21. S. Veprek and J. Vac. Sci. Technol. A, 17[5] (1999) 2401-2420.
22. A. Lasalmonie and J.L. Strudel, J. Mater. Sci. 21[6] (1986) 1837-1852.
23. Y. Kimura, T. Wakabayashi, K. Okada, T. Wada and H. Nishikawa, Wear 232[2] (1999) 199-206.
24. J.L. He, S. Miyake, Y. Setsuhara, I. Shimizu, M. Suzuki, K. Numata and H. Saito, Wear 249[5-6] (2001) 498-502.
25. Y.C. Zhu, K. Fujita, N. Iwamoto, H. Nagasaka and T. Kataoka, Surf. Coat. Technol. 158-159 (2002) 664-668.